Highly ionized xenon and volumetric weighting in restricted focal geometries

J. Strohaber,* A. A. Kolomenskii, and H. A. Schuessler
Florida A&M University, Department of Physics, Tallahassee, Florida 32307, USA and
Texas A&M University, Department of Physics and Astronomy, College Station, Texas 77843-4242, USA
(Dated: July 21, 2015)

The ionization of xenon atoms subjected to 42fs, 800nm pulses of radiation from a Ti:Sapphire laser was investigated. In our experiments a maximum laser intensity of $\sim 2 \times 10^{15}$W/cm^2 was used. Xenon ions were measured using a time-of-flight ion mass spectrometer having an entrance slit with dimensions of 12μm $\times$ 400μm. The observed yields $Xe^{n+}(n = 1 - 7)$ were partially free of spatial averaging. The ion yields showed sequential and nonsequential multiple ionization and dip structures following saturation. To investigate the dip structures and to perform a comparison between experimental and simulated data, with the goal of clarifying the effects of residual spatial averaging, we derived a hybrid analytical-numerical solution for the integration kernel in restricted focal geometries. We simulated xenon ionization using Ammosov-Delone-Krainov and Perelomov-Popov-Terent'ev theories and obtained agreement with the results of observations. Since a large number of experiments suffer from spatial averaging, the results presented are important to correctly interpret experimental data by taking into account spatial averaging.

I. INTRODUCTION

Over the past few decades, research involving the interaction of intense and ultrashort pulsed radiation with matter has become common place and made possible by the advent of chirped-pulse amplification (CPA) [1]. Pulses of radiation generated in a CPA laser have a number of useful properties such as high achievable peak intensities which provide the high optical pumping rates necessary for multiphoton processes as described by lowest order perturbation theory (LOPT) [2], a broadband spectrum having applications in spectroscopy [3], and the production of short pulses used in pump-probe experiments to investigate ultrafast phenomena on the time scale of molecular vibrations [4] and on the time scale of electron dynamics [5]. In the quantitative analysis of the products of laser-matter interactions, a versatile instrument known as a time-of-flight ion mass spectrometer can be used [6]. In these types of experiments, an intense laser beam is focused into a vacuum chamber where it is allowed to interact with chosen target particles. Product ions can then be directed towards a detector such as a multichannel plate (MCP), delay line detector, or Faraday cup for quantification using ion optics.

It was known early on that the production of ions using laser beams resulted in an averaging effect that leads to an $I^{3/2}$ dependence in measured yield curves [7]. This unwanted experimental artifact manifests itself in measuring incorrect relative ion yields between charge states and fragment ions [8], and averaging over structures in intensity dependent ionization yields [9–11]. This process is known in the literature as spatial or intensity averaging, or volumetric weighting [12]. Because of spatial averaging, one does not measure the ionization probability but an averaged result. For researchers in this area, spatial averaging frustrates comparison of experimental data with theoretical results, and many instances can be found in the literature were theoretical results are artificially averaged for comparison [13, 14]. Averaging probabilities tend to make all intensity-dependent ion yield curves similar, and interpretation becomes generic. With the exception of dominating processes such as the nonsequential double ionization of helium, only characteristics such as the order of the multiphoton process and saturation intensity may be determined while the remaining photophysical phenomena are masked.

The potential benefits of intensity-resolved measurements have fueled the development of a plethora of techniques designed specifically for unraveling the masking effects of spatial averaging. These methods can be divided into three groups: pure theoretical [10, 15], pure experimental [6, 16] and combined approaches [8, 12, 17, 18]. Pure theoretical approaches involve mathematical algorithms used to deconvolve experimental data; for instance, researchers working with ion beams typically employ the Abel transformation which allows the Newton sphere to be retrieved. More recently deconvolution of photoelectron yields, in which all electrons in the focus were collected, were performed by a variational approach. As of yet, no purely experimental method has been developed to measure ionization probabilities in above threshold ionization (ATI). However considering ion detection currently, two purely experimental techniques exist that have demonstrated successful results. The first is the photodynamic test tube pioneered by Strohaber [6], and the second is the ion microscope [16]. Finally, mixed methods include intensity-selective scanning ISS [8, 12] and intensity difference scanning IDS [17, 18]. With the exception of the pure theoretical approach many experiments rely on some type of aperture for data collection. This work will provide insight into the effects of volumetric weighting on data, and a complete understanding of the role that volumetric weighting plays in the interaction of radiation with matter in experiments having

* jstroha1@gmail.com

restricted focal geometry.

Due to the large number of possible experimental configurations, their effects on volumetric weighting of data will be considered. Finally, a method with the intent to compare data measured for different experimental configurations is developed. This analysis is largely fuelled by the observation of anomalous structures in measured xenon yields. It has three immediate consequences for research in ionization in strong fields: (i) the ability to correctly interpret experimental data, (ii) to properly spatially average theoretical ionization probabilities for comparison with measured data and (iii) to deconvolve measured data obtained from various focal and slit geometries.

II. EXPERIMENTAL RESULTS ON THE IONIZATION OF XENON

In our ionization experiments with xenon, ultrashort pulses (42 fs) were produces by a Spectra-Physics Spitfire CPA laser having a repetition rate of 1kHz. The radiation had a center wavelength of 800 nm and a pulse energy of 2.5 mJ. Radiation was focused into an ionization chamber by a lens having a nominal focal length of 21 cm. The focused radiation had a minimum beam size of $w_0 = 35.5\mu$m at the $1/e^2$ level, and a Rayleigh range of $z_0 \approx 4.9$ mm. A detailed description of the time-of-flight apparatus is given in [6, 9]. In brief, ions are created within a parallel plate capacitor through photoionization. The produced ions are accelerated into a flight tube where they are subsequently detected by an MCP. By using a combination of spatial (slit) and temporal (time slicing) filtering, ions can be selectively detected from a variable but limited three-dimensional spatial region within the focus.

The backing pressures of both the ionization chamber and flight tube were $\sim 5 \times 10^{-9}$ mbar. Xenon gas having a purity of 99.999% was admitted into the ionization chamber using a precision leak valve (MDC, ULV-150) to a pressure of $\sim 2 \times 10^{-7}$ mbar. Data was recorded using a FAST ComTec counting card (P7886 2-GHz) having a time resolution of 0.5 ns. Data acquisition was automated with LabVIEW code, which measured and adjusted the laser power and recorded experimental parameters and the spectrum. The laser power was attenuated by adjusting a half waveplate positioned before the compressor. For each laser power, the spectrum was averaged over 150,000 laser pulses resulting in a total maximum runtime of 5hrs. The laser powers used in our experiments corresponded to intensities ranging between 4.7×10^{13}W/cm^2 and 2.3×10^{15}W/cm^2. Figure 1 shows the intensity-dependent ionization yields for xenon ions Xe^{n+} $(n = 1 - 7)$ measured with the time of flight apparatus. The data was taken using a slit with dimensions of 400μm along the Rayleigh range and 12μm in the transverse directions. The remaining dimension of the detection volume was unrestricted (no time slicing).

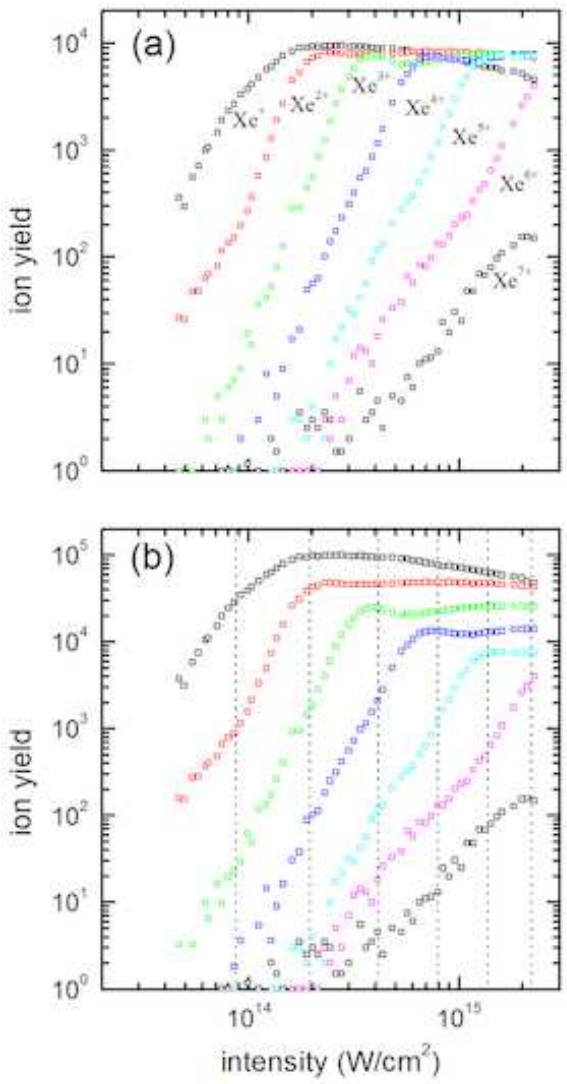

FIG. 1. Ionization yields of xenon using 50fs pulses of radiations centered at 800nm. (a) The yields curves are those of Xe^{n+}, where $n = 1 - 7$. Charges states show clear evidence of nonsequential multiple ionization. Dips in the yield curves following saturation can be seen for charge states 2, 3 and 4. (b) Same as (a) except yields have been vertically displaced by $\times a$, $\times b$, $\times c$, and $\times d$ for Xe^{4+}, Xe^{3+}, Xe^{2+} and Xe^{1+} respectively. Vertical dotted lines indicate saturation intensities determined by OBTI, see text.

The data shown in Fig. 1 is indicative of an sequential ionization process, but also shows contributions from nonsequential multiple ionization. The classical description of over the barrier ionization (OBTI) predicts saturation intensities I_s as the intensity required to lower the field-induced barrier to the energy of the ground state $I_s = 4 \times 10^9 (\mathrm{IE}^4/Z^2)$. Here IE is the ionization energy and Z is the final charge state. Using IEs of [12.13, 20.98 31.05, 42.20, 54.10, 66.70]eV, obtained from the NIST

database [19], the saturation intensities are found to be $[0.87, 1.94, 4.13, 7.93, 13.71, 22.00]\times10^{14}$ W/cm^2. These values are shown by vertical dotted lines in Fig. 1(b). Around $\sim 10^{14}$W/cm^2 a shoulder structure can be seen in the Xe^{2+} ion yields. This shoulder structure saturates near the expected saturation intensity of the respective *previous* charge state Xe^{1+}. Other charge states show indications of nonsequential processes, but we have pointed out the most noticeable one. The data also show a new structure that has not been previously observed. Following saturation of the ion yields of charge states 2, 3 and 4, a dip appears Fig. 1(b). These dips occur near the saturation of the *following* ionic state. It is suspected that the dips are, therefore, formed by the higher nonlinear processes of the subsequent charge states followed by an increase due to spatial averaging and may indicate that the dips are due to a genuine physical process. Since, in general, reducing the effects of spatial averaging (i.e., by restricting the focal volume) produces data that is expected to be more representative of true ionization probabilities, further investigation is required.

To investigate the origin of these dips, we simulated ionization yield curves using ionization rates calculated with the Ammosov-Delone-Krainov (ADK) and Perelomov-Popov-Terent'ev (PPT) theories [20, 21]. While the data in Fig. 1 is to a large degree free of spatial averaging, there remains a residual amount; therefore, to compare with experimental data the theoretical results must be spatially averaged with the volumetric weighting of the detection volume used in the experiment. Previously, an attempt to approximate the kernel [22] for a restricted focal volume was made; however, the results were at best qualitative and thus not suitable for accurate calculations. For these reasons, we have derived a hybrid analytical-numerical solution for the integration kernel and investigated its characteristics and its effects on ionization probabilities. To the best of our knowledge, the kernel for an arbitrary restricted focal geometry has not been presented in the literature and because of its importance in numerous types of experiments, we present results that are general and can be directly applied to a variety of experimental configurations where volumetric weighting is known to obscure results.

III. VOLUMETRIC WEIGHTING FACTORS

When measuring ionization yields in an experiment, the collected ions originate from different locations in the focus, and because the intensity distribution is not uniform (typically taken to be Gaussian), the collected ions are those produced over a broad range of intensities. The ion yields $S(I_0)$ in an experiment at a peak intensity of I_0 is the sum of the products of the probability at a local intensity and the volume of the iso-intensity shell at that intensity. This can be written as the integrated product yield,

$$S(I_0) \propto \int_0^{I_0} P(I) \left| \frac{\partial V}{\partial I} \right| dI. \tag{1}$$

Here $P(I)$ is the actual ionization probability and is the sought after quantity, and $K(I, I_0) = \partial V/\partial I$ is the volumetric weighting factor or integration kernel, a quantity that depends on both the local and peak intensities. The kernel is described completely by the focal geometry. In this work the kernel is taken to be that due to the Gaussian intensity profile,

$$I(z) = I_0 \frac{w_0^2}{w^2(z)} \exp\left(-\frac{2r^2}{w^2(z)}\right). \tag{2}$$

Here w_0 is the waist, $w(z) = w_0(1+z^2/z_0^2)$ is the spot size, and z_0 is the Rayleigh range of the beam. At a specified intensity I, the radius of the corresponding iso-intensity shell as a function of z can be found from Eq. (2),

$$r(z) = w(z)\sqrt{\frac{1}{2}\ln\left|\frac{I_0 w_0^2}{I w^2(z)}\right|}. \tag{3}$$

This expression has the restriction that the natural log under the radical must be greater than or equal to zero, which implies that the natural log argument is greater than one, $I_0 w_0^2 \geq I w^2(z)$. This requirement gives the extent of the iso-intensity shells along the z-direction $z_\pm = \pm z_0\sqrt{I_0/I - 1}$. The volume is then found by integration

$$V_{3D} = \iiint dV = \pi \int_{z_-}^{z_+} r^2(z')dz'. \tag{4}$$

Making use of Eq. (3) and integrating the last expression in Eq. (4) gives,

$$V_{3D} = z_0 w_0^2 \frac{\pi}{9}\Big[\left(\frac{I_0}{I} - 1\right)^{3/2} + 6\left(\frac{I_0}{I} - 1\right)^{1/2} - 6\arctan\left(\sqrt{\frac{I_0}{I} - 1}\right)\Big]. \tag{5}$$

Equation. (5) is the well-known result for the volume within the iso-intensity shells in a Gaussian focus [23].

By restricting the focal volume along the z-direction, usually accomplished by a slit (ISS approach), the volume for this restricted geometry is found by the last integral of Eq. (4) with integration bounds of $z' = z - c/2$ and $z' = z + c/2$,

$$V_{3D}^{FVz} = z_0 w_0^2 \frac{\pi}{18}\Big[3\frac{z}{z_0}\left(3 + \frac{z^2}{z_0^2}\right)\ln\left(\frac{I_0}{I}\frac{z_0^2}{z_0^2 + z^2}\right) + 2\frac{z}{z_0}\left(6 + \frac{z^2}{z_0^2}\right) - 12\arctan\left(\frac{z}{z_0}\right)\Big]_{z-c/2}^{z+c/2}. \tag{6}$$

Here c is the length of the slit in the z-direction. For the given volumes in Eq. (5) and Eq. (6), the associated

kernels found by taking the derivative with respect to intensity are,

$$K_{2D}^{FV}(I, I_0) = \pi \frac{\partial r^2}{\partial I} = \pi \frac{w_0^2}{2I}, \tag{7a}$$

$$K_{3D}^{RVz} = c\left(1 + \frac{z^2}{z_0^2} + \frac{c^2}{12 z_0^2}\right) K_{2D}^{FV}, \tag{7b}$$

$$K_{3D}^{FV} = z_0 \frac{2}{3I}\sqrt{\frac{I_0}{I} - 1}\left(\frac{I_0}{I} + 2\right) K_{2D}^{FV}. \tag{7c}$$

Equation (7a) is the kernel of a 2D slice of zero thickness taken perpendicular through the beam $V_{2D} = \iint dA = \pi r^2$ and is full-view in 2D. The kernel in Eq. (7b) represents a slice of finite extent taken in the transverse direction and centered at position z. This kernel is different than that given in [8, 12]. In [12] the kernel is entirely due to a 2D configuration and this small detail has noticeable effects when computing the kernel in a restricted geometry. Equation (7c) is the full-view kernel in 3D.

IV. VOLUMETRIC WEIGHTING IN RESTRICTED FOCAL GEOMETRIES

In many experiments, a rectangular slit is used to restrict the volume of the focus exposed to the detector. In these cases the volumetric weighting factors are more complex than those given by the analytical expressions in Eq. (7a) and Eq. (7c). To obtain the kernel associated with a 3D detection volume within the focus, we integrate dV in a restricted space over the bounds of a rectangular parallelepiped detection volume. The sides of our detection volume have lengths of a and b in the transverse dimension, and length c in the longitudinal direction. An analytical solution to this integral in terms of elementary functions does not exist, and for this reason we have developed a hybrid analytical-numerical solution obtained by adding up transverse slices of *exact solutions* along the propagation direction. To do this, three different cases must be considered to determine the volume within an iso-intensity shell from a restricted volume. These three cases are illustrated in Fig. 2 with a detection volume of dimensions b(vertical) and a (horizontal).

In Fig. 2(a), iso-intensity shells (circle) with $r < b/2$ are without restriction, in Fig. 2(b) the radius of the iso-intensity shell is greater than $b/2$ but less than $a/2$, in Fig. 2(c) the dection volume is completely enclosed in the iso-intensity shell. Fig. 2(d) is a quadrant view of an intermediate case similar to that shown in Fig. 2(b). For shells completely enclosed [Fig. 2(a)], the volume within the 2D shells is,

$$V_{2D}^{(1)} = \pi r^2. \tag{8}$$

where r is given in Eq. (2). In Fig. 2(c), the shell radius is larger than half the diagonal length $r \geq \sqrt{a^2 + b^2}/2$, and in this case the volume of the iso-intensity shell is equal to the volume of the detection volume $V_{2D}^{(3)} = ab$.

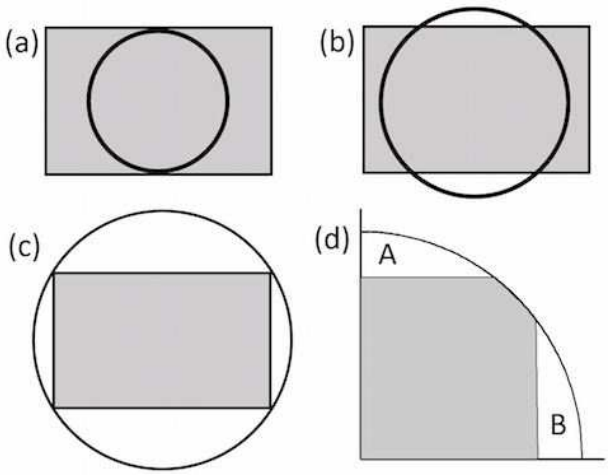

FIG. 2. Two dimensional detection volume and iso-intensity shells. (a) Iso-intensity shell (circle) with diameter smaller than the smallest length of the detection volume (rectangle). (b) iso-intensity shell with diameter larger than one side of the detection volume (intermediate case). (c) isointensity shell with a radius larger than half of the diagonal length of the detection volume. (d) Quadrant view of a intermediate case similar to that in (b) with the detected ions coming from the shaded region. The detection volume is the volume in the iso-intensity shell minus parts A and B.

In the case where the radius of the iso-intensity shell is $(a/2 \text{ or } b/2) \leq r \leq \sqrt{a^2 + b^2}/2$, the volume is more complicated; however, an exact analytical expression can be derived. In Fig. 2(d) a quarter of the detection volume (shaded region) is shown. The detection volume is the volume within the iso-intensity shell (circle) minus four times the volume of parts A and B or $V_{2D}^{(2)} = \pi r^2 - 4V_A - 4V_B$. Part B is the region bounded by the curves $y = \sqrt{r^2 - x^2}$ and $y = 0$, and its volume is found by integrating from $x = a/2$ to $x = r$. Similar analysis can be made for region A and results in the following volumes:

$$V_A = \frac{1}{4}\left[\pi r^2 - a\sqrt{r^2 - \frac{a^2}{4}} - 2r^2 \arcsin\left(\frac{a}{2r}\right)\right], \tag{9a}$$

$$V_B = \frac{1}{4}\left[\pi r^2 - b\sqrt{r^2 - \frac{b^2}{4}} - 2r^2 \arcsin\left(\frac{b}{2r}\right)\right]. \tag{9b}$$

The total restricted volume is therefore

$$V_{2D}^{(2)} = -\pi r^2 + a\sqrt{r^2 - \frac{a^2}{4}} + b\sqrt{r^2 - \frac{b^2}{4}} + 2r^2 \times \left[\arcsin\left(\frac{a}{2r}\right) + \arcsin\left(\frac{b}{2r}\right)\right]. \tag{10}$$

The volumes in Eq.(8) and Eq.(10) together with $V_{2D}^{(3)} = ab$ are plotted (as a function of radius) separately in Fig 3 as the solid blue (region I), red (region II) and black (region III) curves respectively. The dimensions used for

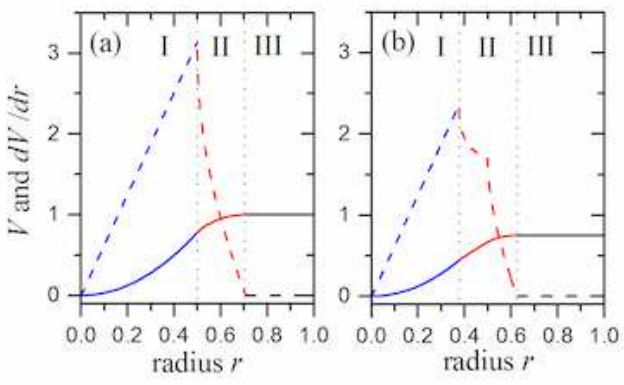

FIG. 3. Detection volume $V(r)$ as a function of radius (solid curve), and derivative of the volume $\partial I/\partial r$ (dashed curve). (a) Volume and its derivative with $a = b = 1$, and (b) volume and derivative with $a = 1$ and $b = 0.75$. Vertical dotted lines separate regions corresponding to different types of restricted volumes.

the volume in Fig. 3(a) are $a = 1$ and $b = 1$, and those in Figs. 3(b) are $a = 1$ and $b = 0.75$. In Figs. 3(a) and (b), the volume (solid blue curve) increases quadratically $V_{2D}^{(1)} = \pi r^2$ until $r = a/2$ in Fig. 3(a) and $r = b/2$ in Fig. 3(b) where the solution of Eq. (10) is plotted (solid red curve). For shells with radii equal to or larger than half the diagonal of the detection volume $r \geq \sqrt{a^2 + b^2}/2$, the volume is constant $V = ab$ (black curve). The derivative $\partial V/\partial I$ is plotted along with the volume to check for consistency and correctness. The kernels $K(I, I_0) = \partial V/\partial I$ associated with these three volumes are,

$$K_{2D}^{(1)} = K_{2D}^{FV}, \tag{11a}$$

$$K_{2D}^{(2)} = K_{2D}^{FV}\left[\frac{2}{\pi}\arcsin\left(\frac{a}{2r}\right) + \frac{2}{\pi}\arcsin\left(\frac{b}{2r}\right) - 1\right], \tag{11b}$$

$$K_{2D}^{(3)} = 0. \tag{11c}$$

When r is equal to or less than the smallest side of the box, the real part of $K_{2D}^{(2)}$ is equal to $K_{2D}^{(1)}$, and when r is greater than the diagonal length of the detection volume $r \geq \sqrt{(a/2)^2 + (b/2)^2}$ the kernel $K_{2D}^{(2)}$ becomes negative and by setting the negative values to zero, the kernel $K_{2D}^{(2)}$ is equal to $K_{2D}^{(3)}$. These conditions mean that Eq. (12) can be rewritten as a single expression,

$$K_{2D}^{RV} = K_{2D}^{FV}\Re\left[\frac{2}{\pi}\arcsin\left(\frac{a}{2r}\right) + \frac{2}{\pi}\arcsin\left(\frac{b}{2r}\right) - 1\right]H_C, \tag{12}$$

where $H_C = H(I - I_C)$ is the Heaviside step function with I_C as the intensity at which the function K_{2D}^{RV} changes sign between positive and negative. This occurs when the detection volume is completely within an iso-intensity shell and its derivative is therefore zero.

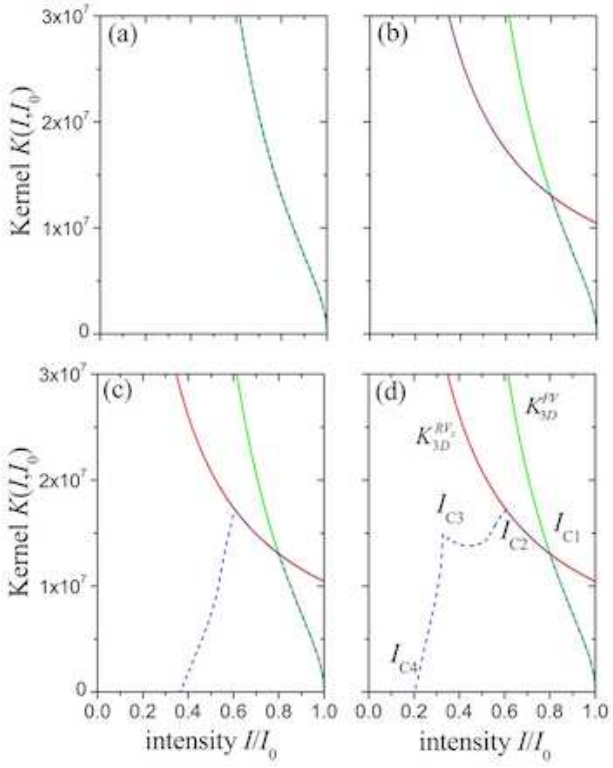

FIG. 4. Theoretically calculated kernels for restricted focal geometries K_{2D}^{RV}. (a) Detection volume dimensions $a = b = 10w_0$ and $c = 10z_0$; (b) $a = b = 10w_0$ and $c = z_0$; (c) $a = b = w_0$ and $c = z_0$; and (d) $a = w_0$, $b = 1.5w_0$ and $c = z_0$. In (a) the dimensions of the detection volume is larger than the iso-intensity shells and $K_{3D}^{RV} \approx K_{3D}^{FV}$ for the plot limits shown. Clipping the iso-intensity shells in the z-direction, K_{3D}^{RV}, within a certain range, will be equal to K_{3D}^{RVz}. For intensities lower than I_{C2}, the kernel K_{3D}^{RV} can take different forms depending on the values of a and b.

For the 3D case, we find the restricted volume by a hybrid analytical-numerical solution where the last dimension is numerically integrated over and from this the kernel L_{3D}^{RV} can be found. In other words, the 3D restricted kernel K_{3D}^{RV} is constructed by adding *exact* two-dimensional volume slices from Eq. (12) in which each 2D volume has a width of Δz determined by the iso-intensity shells. This can symbolically be written as,

$$K_{3D}^{RV} = \sum K_{2D}^{RV}\Delta z. \tag{13}$$

Equation (13) is one of the main results of this work and gives the volumetric weighting factors for a detection scheme with a restricted volume. For simplicity, we have shown Eq. (15) as a Riemann sum; however, in our calculations we employed Simpson's rule and equidistant steps in the z-direction.

V. RESULTS

Figure 4 shows the result of calculations using Eq. (13) for different detection volumes. In Fig. 4(a), the detection volume has the dimensions $a = 10w_0$, $b = 10w_0$ and $c = 10z_0$. This data (dashed blue curve) was plotted along with the exact result (solid green curve) from Eq. (7c), and the two curves lie on top of one another (for the plot limits shown) demonstrating the accuracy of the calculation. At the peak intensity $I = I_0$, the kernel goes to zero, as it must for *all* possible slit geometries. If K_{3D}^{FV} did not go to zero here, then the calculations would result in incorrect interpretation of further analysis. In Fig 4(b), the slit values have been taken to be $a = 10w_0$, $b = 10w_0$ and $c = z_0$. It can be seen that the K_{3D}^{FV} (green) and K_{3D}^{RVz} (solid red curve) curves cross at an intensity of $I = 0.8I_0$. Here the calculated kernel K_{3D}^{RV} (dashed blue curve) is plotted along with K_{3D}^{FV} and K_{3D}^{RVz} and follows K_{3D}^{FV} until an intensity of $I = 0.8I_0$, afterward following K_{3D}^{RVz}(red curve) for the lower intensities. In Fig. 4(c), the dimensions of the detection volume are $a = w_0$, $b = w_0$ and $c = z_0$. This situation is similar to that shown in Fig. 4(b), except that the calculated kernel deviates from K_{3D}^{RVz} at an intensity of $I = 0.61I_0$ and goes to zero at $I = 0.36I_0$. Lastly, in Fig. 4(d), the slit dimensions are $a = w_0$, $b = 1.5w_0$ and $c = z_0$. This is similar to the data shown in Fig. 4(c), except that the curve after $I = 0.61I_0$ peaks again around $I = 0.32I_0$ and then goes to zero at $I = 0.22I_0$. This analysis shows that the results are in excellent agreement with the known analytical results of Eq. 7(b) and Eq. 7(c) and provides assurance of similar accuracy for the remaining portion of the curves. The calculated kernel K_{3D}^{RV} can be further quantified by determining critical intensities at which the kernel changes geometries as previously discussed. This is the topic of the next section.

VI. CRITICAL INTENSITIES

In Fig. 4(d), four critical intensities are shown. The dimensions used for the calculated kernel were $a = w_0$, $b = 1.5w_0$ and $c = z_0$. The first critical intensity occurs when the kernel changes from K_{3D}^{FV} to K_{3D}^{RVz}. The kernel K_{3D}^{FV} came about from integration over all space (no restriction) and K_{3D}^{RVz} was calculated by restricting integration along the z-axis. This suggests that the change in geometry of the kernel is due to clipping of the iso-intensity shells along the z-direction. To quantify this, the local on-axis intensity $I_{0L} = I_0 w_0^2/w^2$ is calculated at the position $z = c$. The intensity found in this way is $I_{C1} = I_0/(1 + c^2/z_0^2)$, and for the detection volume used in Fig. 4(d) it is $I_{C1} = 0.81I_0$. This is the intensity in which the kernel K_{3D}^{RV} changes from that of Eq. (7b) to (7c) due to clipping of the iso-intensity shells in the z direction.

The next critical intensities occur when the largest radius $r(z)$ of a shell meets the transverse dimension of the detection volume. The critical intensity at $0.61I_0$ occurs because the largest radius of the iso-intensity shell is equal to half the dimension of the smallest transverse length (in this case a) of the detection volume. Plugging $r = a/2$ and $z = 0$ into Eq. (2), the critical intensity is found to be $I_{C2} = I_0 \exp(-a^2/w_0^2/2) = 0.6065I_0$. The same analysis can be applied to the largest transverse slit dimension $b = 1.5w_0$ and gives an intensity of $I_{C3} = I_0 \exp(-b^2/w_0^2/2) = 0.3247I_0$. The largest transverse radius $r(z)$ occurs when the derivative is equal to zero, $dr/dz = 0$. In this way the largest radius occurs at the positions $z = 0$ and $z = \pm\sqrt{I_0 e^{-1}/I - 1}$. This last expression is real for intensities $I \leq I_0 e^{-1}$, and the isointensity shells take the peanut shapes shown in Fig 6. When $I \geq I_0 e^{-1}$ the term under the radical is less than zero and all iso-intensity shells have an elliptical shape with a maximum at $z = 0$. The boundary between the peanut and elliptically shaped iso-intensity shells is shown by the dotted contour in Fig. 5.

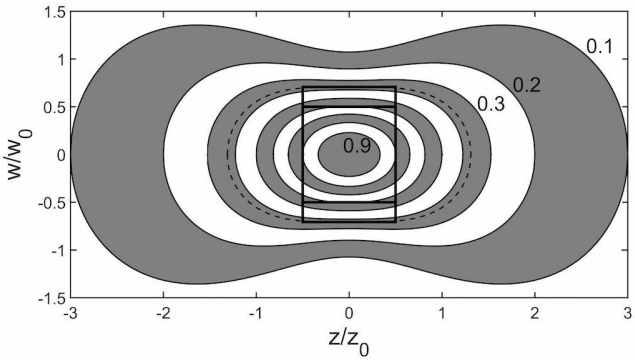

FIG. 5. Isointensity contours and detection volume. The black lines are iso-intensity contours with heights ranging from $0.1I_0$ to $0.9I_0$ in increments of $0.1I_0$. These contours are either elliptically-shaped with a single maximum at $z = 0$, or peanut-shaped with two maxima $z = \pm\sqrt{I_0 e^{-1}/I - 1}$. The intensity that separates the elliptical shapes from the peanut shapes is $I = I_0 e^{-1}$ and is shown by the dotted line. The small box represents a detection volume with sides $a = b = w_0$, and $c = z_0$. The larger box is the same as the small box but rotated by 45° and projected onto the yz-plane.

Lastly at the lower intensities, isointensity shells can be found such that the detection volume is completely enclosed within it. The highest intensity for which this situation occurs is when the radius of the shell is at the corner of the detection volume at $z = c$. To find this intensity, the bracketed expression in Eq. (12) is set to zero, which is motivated by the fact that this results in $K_{3D}^{RV} = 0$. This procedure gives the intensity

$$I_{C4} = I_0 \frac{1}{1 + c^2/z_0^2} \exp\left(-\frac{1}{2}\frac{a^2 + b^2}{1 + c^2/z_0^2}\right), \qquad (14)$$

which for our example gives $I_{C4} = 0.2180I_0$.

In conclusion of this section, while one of the goals of this work was to analyze the origin of the dips in the measured xenon data, our previous work [10] suggested that

if a kernel could be found for a restricted focal geometry, then it may be possible to remove residual spatial averaging. That method employed a power series expansion of both the experimental yield $S(I_0)$ and probability $P(I)$ data,

$$S(I_0) = I_0^{m-1} \sum_k A_k I_0^k, \tag{15a}$$

$$P(I) = I^{m-1} \sum_k \frac{A_k}{G_k} I^k. \tag{15b}$$

Here k is the expansion index, m can be taken to be the lowest possitive integer value that results in a solution to the Volterra equation, Eq. (1) (for 1D and 2D geometries $m = 1$ and for 3D geometries $m = 3$), A_k are expansion coefficients of the yield $S(I_0)$ and the G_k are geometric factors determined by the integrated kernel,

$$G_k \propto \int_0^1 K_{ND}(\xi) \xi^{k+m-1} d\xi. \tag{16}$$

In [10], the kernels $K(\xi)$ were given for the 1D, 2D and 3D cases; however, in practice the kernels are all 3D and for the kernels given in Eq. (7b) and Eq. (7c) the geometric factors are

$$G_k^{FV} = \pi z_0 w_0^2 N \frac{\sqrt{\pi}}{3} \left[\frac{\Gamma(k+m-5/2)}{2\Gamma(k+m-1)} + \frac{\Gamma(k+m-3/2)}{\Gamma(k+m)} \right], \tag{17a}$$

$$G_k^{FVz} = \pi z_0 w_0^2 N \frac{1}{3} \left(\frac{c^2}{z_0^2} + 3 \right) \frac{1}{k+m-1}, \tag{17b}$$

where N is the particle density and Γ is the gamma function. To perform the deconvolution, the spatially averaged experimental data $S(I_0)$ is expanded in a power series according to Eq. (15a) to obtain the expansion coefficients A_k. The geometric factors G_k are then determined using Eq (16) with the appropriate volumetric weighting factor K. Equation (17) are analytical expressions for the G_k in three dimensional geometries. This work, however, has provided a kernel for restricted focal geometries Eq. (13) and once calculated using the method outlined here, it can be integrated in Eq. (16) to find the geometric factors. We also note that the kernel K_{3D}^{RV} may contain parts from K_{3D}^{FV} and K_{3D}^{RVz} which have known solution to Eq. (16). Once the geometric factors are determined, they can be used along with the A_k in Eq. (15b) to recover the ionization probability $P(I)$ in a power series expansion using the new expansion coefficients A_k/G_k.

VII. COMPARISON WITH EXPERIMENTAL DATA

In this section we investigate the effects of spatial averaging on measured ion yields curves. To do this, we calculated ionization rates W using ADK and PPT theories to generate ionization curves of Xe. Figures 6(a), and 6(b) show the results of the simulated ion yields of xenon up to the seventh charge state. The simulated yields have only a contribution from sequential ionization and show agreement with the data only near saturation. In Fig. 6(a), the measured Xe^{2+} deviates from the the calculated yield at an intensity of $\sim 10^{14}$W/cm^2. This intensity corresponds with the saturation intensity of Xe^{1+} and for this reason the Xe^{1+} yields have been shifted up by a factor of 3 times. For comparison with the experimental yields, the simulated yields were spatially averaged using slit dimensions of $a = 12\mu$m, $b = \infty$ in the transverse

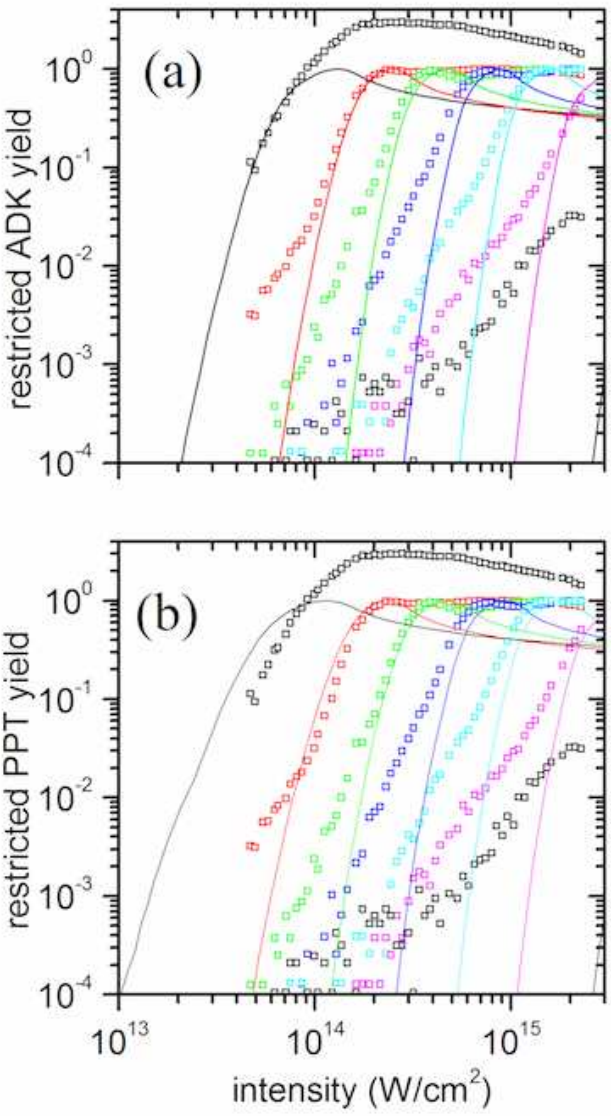

FIG. 6. Ionization yields of Xe^{n+} ($n = 1-7$). (a) Ionization probabilities calculated using ADK theory (solid curves), and measured ionization yields using a detection volume of dimensions $a = 12\mu$m by $b = \infty$ by $c = 400\mu$m(squares). (b) Same as (a) except the probability was calculated using PPT theory.

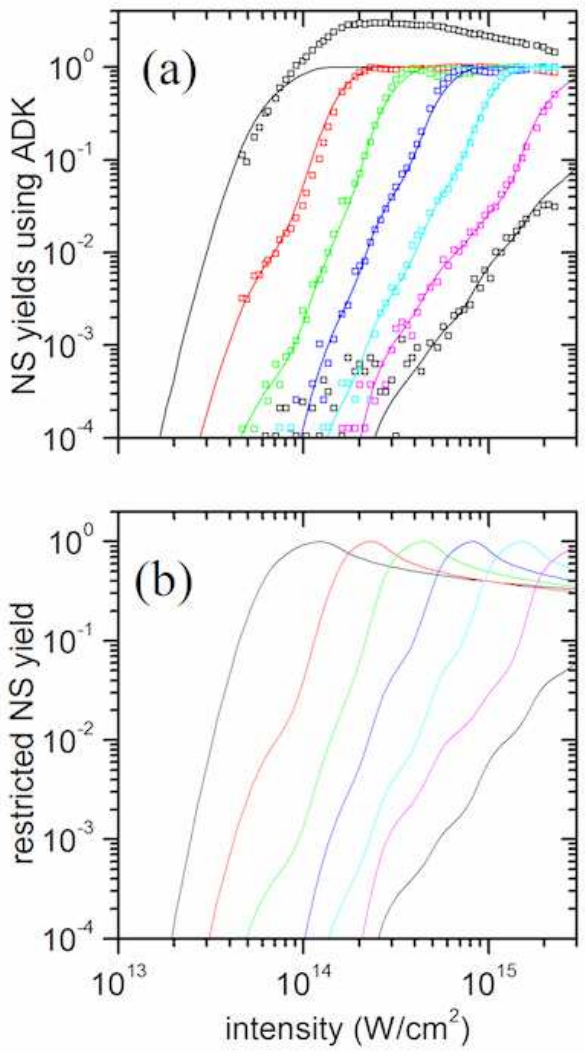

FIG. 7. Spatial averaged nonsequential ionization yields of Xe^{n+} ($n = 1-7$). (a) Simulated nonsequential yields spatially averaged using a detection volume with dimensions $a = \infty$ by $b = \infty$ by $c = 400\mu$m. (b) Simulated nonsequential yields spatially averaged using our experimental detection volume with dimension of $a = 12\mu$m by $b = \infty$ by $c = 400\mu$m. The simulated nonsequential portion of a particular charge state was found by weighting the ADK rates used for previous charge states (see text).

dimension and $c = 400\mu$m along the propagation direction. The simulated averaged yields decrease following saturation but do not increase afterwards as seen in the experiment data.

For better comparison with the data, nonsequential ionization probabilities were simulated by weighting ADK rates of previous charge states according to,

$$\frac{dN_n}{dt} = \sum_{j=0}^{n-1} \alpha_{j,n} W_{j,n}^{ADK} N_j - \sum_{k=n+1} \alpha_{n,k} W_{n,k}^{ADK} N_n. \quad (18)$$

Here N_n is the poplution of the n^{th} charge state i.e., N_0 is the population of the neutral atoms, the $W_{i,j}$ are the sequential ionization rates determined by ADK, and the $\alpha_{i,j}$ are the nonsequential ionization coefficients[23]. The indices on $\alpha_{i,j}$ and $W_{i,j}$ reads from the i^{th} charge state to the j^{th} charge state. For the neutral charge state, the first sum in Eq. (18) is zero and the rate equation for the neutral population has the analytical solution $N_0 = \exp(-\sum W_{0,k} t)$. Higher order charge state populations were found by numeric integration. The nonsequential ionization coefficients were found by fitting the simulated yields to the experimentally obtained data. Their values are shown in table I. When all coefficients are zero, except those that are unity, the rate equations lead to sequential ionization yields. The nonsequential yield are shown in Fig. 7(a) and can be contrasted with those in Fig. 6 in which the simulated yields were calculated in a sequential manner. Since the experimental data is relatively flat following saturation, we spatially averaged the simulated probabilities using Eq. (7a) to achieve a better fit. The simulated probabilities were than spatially averaged using the dimensions of the detection volume used in our experiment. This simulated data is plotted in Fig. 7(b). As in the case when ADK and PPT theories were used a decrease following saturation can be seen, but does not increase afterwards. Different slit geometries were investigated, however, complete agreement with the data in Fig. 1 could not be found. Comparison of the results with experiment suggests that the dips in the yield curves may arise from residual spatial averaging.

TABLE I. Coefficients of $\alpha_{i,j}$ of the NS ionization of xenon

				j			
i	1	2	3	4	5	6	7
0	1	0.0001	0.000045	—	—	—	—
1		1	0.03	0.0035	0.0004	—	—
2			1	0.065	0.006	0.003	0.0003
3				1	0.08	0.015	0.0009
4					1	0.04	0.0068
5						1	0.025
6							1

Finally, we attempted to reconstructed the ionization probabilities using Eqs. (15-17) with the kernel derived in Eq. (13). The level of noise in the experimental data was such that this technique failed to retrieve the probability; however, we developed a new technique in which the ionization probability at a particular intensity I_0 is found from an initial guess. This initial guess was then spatially averaged using Eq. (1) and Eq. (13), and the difference between the simulated signal $Y(I_0)$ and the actual experimental signal $S(I_0)$ was calculated. Based on this difference, a new guess for $P(I_0)$ was made. This

procedure was repeated until a minimum distance was reach between the experimental signal and the simulated signal according to,

$$S(I_0) - C\int_0^{I_0} K(I_0, I)P(I)dI \leq \beta S(I_0). \qquad (19)$$

Here the second term on the left is the simulated signal $Y(I_0)$ with C as a proportionality constant in Eq. (1), and β is a closeness parameter. In our simulations β was taken to be equal to 10^{-4} of the experimental value $S(I_0)$.

Figure 8 shows the results of this new deconvolution procedure. The retrieved Xe charge states are as indicated in Fig. 1. The solid black curve is the sum of all charge state probabilities. For charge states up to Xe^{5+}, a decrease in probability is seen following saturation as expected from a sequential ionization process. The initial decrease in their probabilities are followed by a region where the probabilities "stabilize" before further decreasing. This decrease and "suppression" in the retrieved ionization probabilities result in the dips observed in the experimental yield curves. The origin of this phenomenon is not known to us, but the structure partially survives the masking effect of spatial averaging in the restricted focal geometry. The integration kernel in Eq. (13) assumes a Gaussian focal geometry and as a result the deconvolution is strongly dependent on the form of the focal geometry. While the retrieved ionization probabilities may suffer from imprecise knowledge of the focal intensity profile, we are convinced that the results are consistent with the measured data for two reasons. First, in a 2D detection scheme such as ISS, the yield curves will always be monotonically increasing functions. The fact that we observe a decrease following saturation indications that our detection volume is more restricted than that of a 2D detection volume. Secondly, any increase in the yields following a decrease can only occur if the probability stabilizes or increases. The structures in the yield curves are therefore consistent with the retrieved probabilities.

VIII. CONCLUSIONS

Highly ionized xenon atoms were measured as a function of intensity up to the seventh charge state. Sequential as well as nonsequential ionization processes were observed in the yields curves. A dip structure was observed in some of the yield curves following saturation where the following charge state has a significant yield. To investigate the dips, we derived for the first time the integration kernel K_{3D}^{RV} for restricted focal geometries. These kernels were used to spatially average simulated ion yields using ADK and PPT theories, and the results partially suggested that the dips may be due to residual spatial averaging. The inclusion of nonsequential multiple ionization had little effect on the spatially averaged curves following saturation. Retrieved probabilities curves found using a new deconvolution technique and the restricted kernel indicate that the dips may be due to a genuine photophysical process.

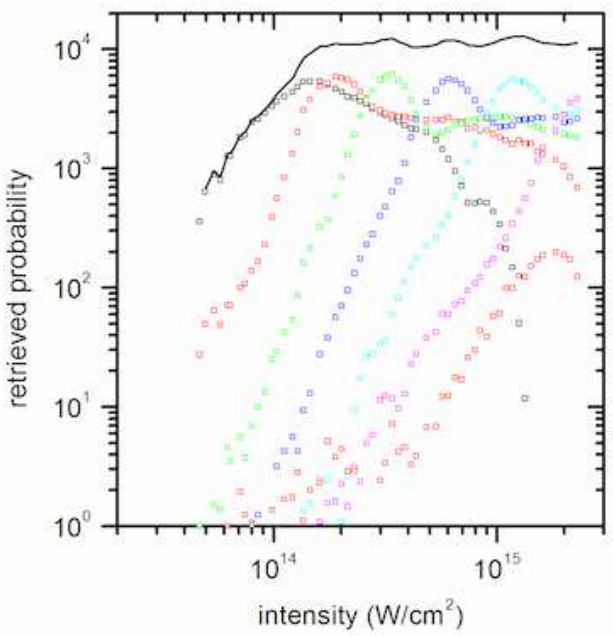

FIG. 8. Retrieved ionization probabilities of Xe charge states. Each charge state is denoted as in Fig. 1. The solid black curve is the sum of all charged states probabilities. For charge states that have reached saturation, a decrease in the probability is observed. The retrieved data shows that the probabilities do not contiuously decrease as expected by the continuous increase in probability of the following charge state but "stabilize" for some range of intensities before decreasing.

ACKNOWLEDGMENTS

This work was funded by the Robert A.Welch Foundation, Grant No. A1546 and the Qatar Foundation under Grant No. NPRP 5-994-1-172. Special thanks to Timothy Scarborough for laboratory maintenance.

[1] D. Strickland and G. Mourou, Opt. Commun **56**, 219 (1985).

[2] S. L. Chin, C. Rolland, P. B. Corkum, and P. Kelly, Phys. Rev. Lett. **61**, 153 (1988).

[3] F. Zhu, H. Hundertmark, A. A. Kolomenskii, J. Strohaber, R. Holzwarth, and H. A. Schuessler, Opt. Lett. **38**, 2360 (2013).
[4] A. H. Zewail, J. Phys. Chem. **104**, 5660 (2000).
[5] M. Uiberacker, Nature **446**, 627 (2007).
[6] J. Strohaber and C. Uiterwaal, Phys. Rev. Lett. **100**, 023002 (2008).
[7] S. Speiser and J. Jortner, Chem. Phys. Lett. **44**, 399 (1976).
[8] P. Hansch, M. A. Walker, and L. D. V. Woerkom, Phys. Rev. A **54**, R2559 (1996).
[9] J. Strohaber, T. Mohamed, N. Hart, F. Zhu, R. Nava, F. Pham, A. A. Kolomenskii, H. Schroeder, G. G. Paulus, and H. A. Schuessler, Phys. Rev. A **84**, 063414 (2011).
[10] J. Strohaber, A. A. Kolomenskii, and H. A. Schuessler, Phys. Rev. A **82**, 013403 (2010).
[11] T. D. Scarborough, J. Strohaber, D. B. Foote, C. J. McAcy, and C. J. G. J. Uiterwaal, Phys. Chem. Chem. Phys. **13**, 13783 (2011).
[12] M. Walker, P. Hansch, and L. V. Woerkom, Phys. Rev. A **57**, R701 (1998).
[13] K. Nagaya, K. Mishima, H.-F. Lu, M. Hayashi, and S. Lin, Chem. Phys. Lett. **424**, 34 (2006).
[14] A. S. Kornev and B. A. Zon, Phys. Rev. A **86**, 043401 (2012).
[15] N. A. Hart, J. Strohaber, G. Kaya, N. Kaya, A. A. Kolomenskii, and H. A. Schuessler, Phys. Rev. A **89**, 053414 (2014).
[16] M. Schultze, B. Bergues, H. Schroder, F. Krausz, and K. L. Kompa, New J. Phys. **13**, 033001 (2011).
[17] E. P. Benis and et al, Phys. Rev. A **70**, 025401 (2004).
[18] P. Wang, A. M. Sayler, K. D. Carnes, B. D. Esry, and I. Ben-Itzhak, Opt. Lett. **30**, 664 (2005).
[19] NIST, "Nist atomic spectra database ionization energies data," (2015).
[20] F. Yan-Zhuo, Z. Song-Feng, and Z. Xiao-Xin, Chin. Phys. B , 113101 (2012).
[21] A. M. Perelomov, V. S. Popov, and M. V. Terentev, J. Exptl. Theoret. Phys. **50**, 1393 (1966).
[22] T. Scarborough and C. J. G. J. Uiterwaal, Laser Phys. **23**, 125302 (2013).
[23] S. Augst, D. D. Meyerhofer, D. Strickland, and S. L. Chin, J. Opt. Soc. Am. B **8**, 858 (1991).